

# Global $\Lambda$ polarization in heavy-ion collisions at high baryon density

Yu. B. Ivanov<sup>1,2,\*</sup>

<sup>1</sup>*Bogoliubov Laboratory for Theoretical Physics, Joint Institute for Nuclear Research, Dubna 141980, Russia*

<sup>2</sup>*National Research Centre "Kurchatov Institute", Moscow 123182, Russia*

Based on the model of three-fluid dynamics (3FD), the global  $\Lambda$  polarization ( $P_\Lambda$ ) is calculated in Au+Au collisions at  $3 \leq \sqrt{s_{NN}} \leq 9$  GeV, in which high baryon density is achieved. Various contributions to  $P_\Lambda$  are considered: those from the thermal vorticity, meson field, thermal shear and spin-Hall effect. Feed-down from higher-lying resonances is also taken into account. The results are compared with available data. Special attention is paid to the collision energies of  $\sqrt{s_{NN}} = 3, 3.2, 3.5, 3.9$ , and  $4.5$  GeV, for which a thorough scan of the energy, rapidity, and centrality dependence of  $P_\Lambda$  is performed. The results for 3 GeV reasonably well reproduce the corresponding STAR data. While the results at  $\sqrt{s_{NN}} = 3.2, 3.5, 3.9$ , and  $4.5$  GeV can be considered as predictions for results of measurements within the STAR fixed-target (STAR-FXT) program that are expected in the nearest future. It is predicted that a broad maximum of  $P_\Lambda$  is reached at  $\sqrt{s_{NN}} \approx 3\text{--}3.9$  GeV, exact position of which depends on the centrality and width of the midrapidity range of observation. Impact of the meson-field, thermal-shear and spin-Hall-effect contributions to  $P_\Lambda$  is also studied.

PACS numbers: 25.75.-q, 25.75.Nq, 24.10.Nz

Keywords: relativistic heavy-ion collisions, hydrodynamics, polarization

## I. INTRODUCTION

Non-central heavy-ion collisions are characterized by huge angular momenta of the order of  $10^3\text{--}10^4\hbar$ . Although a part of the angular momentum is carried away by spectators, a large fraction of it remains in the participant region of the colliding nuclei and induces collective vortical motion of the participant matter. This vortex motion is partially transformed into a preferential orientation of spins of the participant particles through spin-orbit coupling, which can be observed as a polarization (for fermions) or alignment (for vector mesons) of emitted particles. Observation of this polarization (alignment) gives us access to information about the vortex motion during heavy-ion collisions, provided the mechanism of partial transformation of the collective vortex motion into the spin polarization (alignment) is understood. The current state of theoretical and experimental research in this area is discussed in recent reviews [1, 2].

Measurements of the global polarization of the  $\Lambda$  and  $\bar{\Lambda}$  hyperons by the STAR Collaboration at collision energies  $7.7 \leq \sqrt{s_{NN}} \leq 39$  GeV and at  $\sqrt{s_{NN}} = 200$  GeV showed statistically significant result [3, 4]. These measurements demonstrated a rising global polarization with decreasing  $\sqrt{s_{NN}}$ . A simple extrapolation of this trend would suggest that the global polarization continues to rise as  $\sqrt{s_{NN}}$  decreases. However, the global polarization should vanish at  $\sqrt{s_{NN}} = 2m_N$  ( $m_N$  is the nucleon mass) due to zero angular momentum of the system at this energy. Therefore, a peak of the global polarization should occur in the region  $2m_N < \sqrt{s_{NN}} \leq 7.7$  GeV, where high baryon density is reached.

Various predictions for the global  $\Lambda$  polarization ( $P_\Lambda$ )

at  $\sqrt{s_{NN}} < 7.7$  GeV were done [5–10]. The maximum  $P_\Lambda$  has been predicted around 7.7 GeV in Ref. [9] while the averaged thermal vorticity, i.e. the driving force of the polarization, was reported to reach a peak at around 3–4 GeV [5, 9]. Calculations of Refs. [6–8, 10] predicted monotonous rise (with decreasing  $\sqrt{s_{NN}}$ ) up to  $\approx 3$  GeV. Ref. [10] reported almost constant  $P_\Lambda$  from 7.7 to  $\approx 3$  GeV and then rapid rise to maximum at  $\sqrt{s_{NN}} = 3$  GeV followed by rapid fall to zero.

The STAR [11] and HADES [12] data on  $P_\Lambda$  at  $\sqrt{s_{NN}} = 3$  GeV and  $\sqrt{s_{NN}} = 2.4$  GeV, respectively, showed that predictions of Refs. [8, 10] capture the experimental trend. These data demonstrated that increase of  $P_\Lambda$  with decreasing  $\sqrt{s_{NN}}$  continues below 7.7 GeV and indicated that the peak in  $P_\Lambda$  is reached definitely below the energy of 7.7 GeV. However, the questions remained: is it a gradual increase from 7.7 to 3 GeV or with a peak in between, or is it a slow increase to 3 GeV and then steep fall [10]? As aforementioned, these different scenarios reflect different patterns of the collective vortical motion in the produced nuclear matter. These different patterns in particular lead to differences in rapidity dependence of  $P_\Lambda$  [9, 13].

In Ref. [13], the calculations in the energy range  $2.4 < \sqrt{s_{NN}} < 7.7$  GeV has been already performed but it was not a thorough scan of this energy range. The main purpose of Ref. [13] was to study meson-field induced contribution to the global polarization proposed in Ref. [14], see also [15], and its application to description of data at  $\sqrt{s_{NN}} = 2.4, 3$  and  $7.2$  GeV [11, 12, 18]. Recently it has been found that there are an additional contributions to the spin polarization at local equilibrium [2, 19–22]. These are a so-called thermal-shear and spin-Hall-effect contributions, which await evaluation in the STAR-FXT energy range.

In the present paper, the global  $\Lambda$  polarization is calculated in Au+Au collisions at  $3 \leq \sqrt{s_{NN}} \leq 9$  GeV. Special

\*e-mail: yivanov@theor.jinr.ru

attention is paid to the collision energies of  $\sqrt{s_{NN}} = 3, 3.2, 3.5, 3.9,$  and  $4.5$  GeV, for which a thorough scan of the energy, rapidity, and centrality dependence of  $P_\Lambda$  is performed. Effects of the thermal-shear and spin-Hall-effect contributions [20, 21] to  $P_\Lambda$  are also studied. These simulations closely follow the procedure described in Ref. [13]. The obtained results at energies of 3.2–4.5 GeV can be considered as a prediction for the STAR-FXT experimental data that are expected in the nearest future. These results are also relevant to forthcoming experiments at Nuclotron-based Ion Collider fAcility (NICA) in Dubna (BM@N and MPD experiments).

## II. GLOBAL POLARIZATION IN 3FD MODEL

The scheme of the  $P_\Lambda$  calculation is precisely the same as that described in Ref. [13]. In Ref. [13] two contributions to the global  $\Lambda$  polarization were considered. The first one is the conventional contribution associated with the thermal vorticity

$$\varpi_{\mu\nu} = \frac{1}{2}(\partial_\nu\beta_\mu - \partial_\mu\beta_\nu). \quad (1)$$

Here  $\beta_\mu = u_\nu/T$ ,  $u_\mu$  is collective local four-velocity of the matter, and  $T$  is local temperature. Here we deal with  $u_\mu$  and  $T$  of the unified fluid in terms of the 3FD model because the system is equilibrated at the freeze-out stage. It is instructive to divide thermal vorticity into kinematic vorticity,  $\omega_{\mu\nu}$ , and vorticity due to  $1/T$  derivatives,  $\omega_{\mu\nu}^{(T)}$

$$\varpi_{\mu\nu} = \omega_{\mu\nu} + \omega_{\mu\nu}^{(T)}, \quad (2)$$

where

$$\omega_{\mu\nu} = \frac{1}{2T}(\partial_\nu u_\mu - \partial_\mu u_\nu), \quad (3)$$

$$\omega_{\mu\nu}^{(T)} = \frac{1}{2}(u_\mu\partial_\nu - u_\nu\partial_\mu)\frac{1}{T}. \quad (4)$$

The corresponding mean spin vector of  $\Lambda$  particles with four-momentum  $p$ , produced around point  $x$  on freeze-out hypersurface is

$$S_\mu^\varpi(x, p) = \frac{1}{8m_\Lambda}[1 - f_\Lambda(x, p)]\epsilon_{\mu\nu\rho\sigma}p^\sigma\varpi^{\rho\nu}(x) \quad (5)$$

where  $f_\Lambda(x, p)$  is the Fermi-Dirac distribution function and  $m_\Lambda$  is mass of the  $\Lambda$  hyperon. Further on, the Fermi factor  $[1 - f_\Lambda(x, p)]$  is omitted because the  $\Lambda$ 's are produced in high-temperature regions, where Boltzmann statistics dominates.

The second, less conventional contribution, considered in Ref. [13], is related to the meson-field contribution [14, 15]. The corresponding mean spin vector is

$$S_\mu^V(x, p) = \frac{1}{8m_\Lambda}\epsilon_{\mu\nu\rho\sigma}p^\sigma\left(\beta_\Lambda\frac{g_{V\Lambda}}{m_\Lambda T}\right)V^{\rho\nu}, \quad (6)$$

where the Fermi factor  $[1 - f_\Lambda(x, p)]$  is again omitted,  $\beta_\Lambda = 1$  [note that  $\beta_{\bar{\Lambda}} = -1$ ],  $g_{V\Lambda}$  is coupling constant of the vector meson with  $\Lambda$  hyperon,

$$V_{\mu\nu} = \partial_\mu V_\nu - \partial_\nu V_\mu \quad (7)$$

is the vector-field strength tensor, and the  $V$  field itself is defined as

$$V^\nu = \frac{\bar{g}_V}{m_V^2}J_B^\nu \quad (8)$$

through the baryon current  $J_B^\nu = n_B u^\nu$ ,  $n_B$  is the baryon density,  $m_V$  is the vector-meson mass, and  $\bar{g}_V$  is the mean coupling constant of the vector meson with various baryons. The vector-meson-field contribution (6) is similar to that of the electromagnetic field interacting with magnetic moment of the hyperon [26].

The meson-field contribution to the mean spin vector (6) was derived in Ref. [14, 15] based on the relativistic mean-field (RMF) model [16], where the vector meson is associated with the  $\omega$  meson. Therefore  $m_V = m_\omega = 783$  MeV. Values of coupling constants differ in different realizations of the RMF model. Following Refs. [14, 15], we use just one of the possible parametrizations:  $\bar{g}_V = g_{VN} = 8.646$  and  $g_{V\Lambda} = 0.67g_{VN}$  [17]. The mean coupling constant is associated with the nucleon one because nucleons dominate in the system at low energies considered here.

The polarization of the  $\Lambda$  hyperon is measured in its rest frame, therefore the  $\Lambda$  polarization is

$$\Pi_\Lambda^\mu(x, p) = S^{*\mu}(x, p)/S_\Lambda \quad (9)$$

where  $S_\Lambda = 1/2$  is the spin of the  $\Lambda$  hyperon and  $S_\Lambda^{*\mu}$  is mean  $\Lambda$ -spin vector in its rest frame. The zeroth component  $S_\Lambda^0$  identically vanishes in the  $\Lambda$  rest frame. We are interested in  $y$  component of  $\Pi_\Lambda^\mu$  because the global polarization is directed orthogonally to the reaction plane ( $xz$ ).

Particles are produced across entire freeze-out hypersurface. Therefore, to calculate the global polarization ( $P_\Lambda$ ), the above expression should be averaged over the freeze-out hypersurface  $\Sigma$  and particle momenta

$$P_\Lambda = \frac{\int(d^3p/p^0)\int_\Sigma d\Sigma_\lambda p^\lambda f_\Lambda \Pi_\Lambda^y}{\int(d^3p/p^0)\int_\Sigma d\Sigma_\lambda p^\lambda f_\Lambda}. \quad (10)$$

In principle, the integration over momenta should run over the range of the experimental acceptance. However, we integrate over all momenta, but the experimental rapidity acceptance is approximately taken into account in terms of a so-called hydrodynamical rapidity

$$y_h = \frac{1}{2}\ln\frac{u^0 + u^3}{u^0 - u^3}, \quad (11)$$

based on hydrodynamical 4-velocity  $u^\mu$ . It means that the  $d\Sigma_\lambda p^\lambda$  integration runs only over part of the freeze-out hypersurface, where condition  $|y_h| < y_{\text{acceptance}}$  is

met. This part the hypersurface is denoted as  $\Sigma_{\Delta y}$ . Similarly to previous 3FD calculations of the  $\Lambda$  polarization [6–8, 13], a simplified version of the freeze-out is used, i.e. an isochronous one. The freeze-out instant is taken to be equal to that, when the average energy density in the central region (i.e. slab  $|z| \leq 4$  fm) drops down to the value of the average freeze-out energy density in the same central region obtained in conventional 3FD simulations with differential, i.e. cell-by-cell, freeze-out [29, 30].

Performing integration over  $dp$  as it is described in Ref. [13] in detail, we arrive to the following expressions for thermal-vorticity ( $P_\Lambda^\varpi$ ) and meson-field ( $P_\Lambda^V$ ) contributions to the global  $\Lambda$  polarization:

$$P_\Lambda^\varpi = \frac{1}{6} \frac{\int_{\Sigma_{\Delta y}} d^3x (\rho_\Lambda + 2T_\Lambda^{00}/m_\Lambda) \varpi_{zx}}{\int_{\Sigma_{\Delta y}} d^3x \rho_\Lambda}, \quad (12)$$

$$P_\Lambda^V = \frac{\beta_\Lambda g_{V\Lambda}}{6m_\Lambda T} \frac{\int_{\Sigma_{\Delta y}} d^3x (\rho_\Lambda + 2T_\Lambda^{00}/m_\Lambda) V_{zx}}{\int_{\Sigma_{\Delta y}} d^3x \rho_\Lambda}, \quad (13)$$

where  $\rho_\Lambda$  is the  $\Lambda$  density in the frame of calculation and  $T_\Lambda^{00}$  is the 00 component of the partial energy-momentum tensor related to the  $\Lambda$  contribution

$$T_\Lambda^{\tau\lambda} = (\varepsilon_\Lambda + p_\Lambda) u^\tau u^\lambda - g^{\tau\lambda} p_\Lambda \quad (14)$$

with  $\varepsilon_\Lambda$  and  $p_\Lambda$  being the corresponding partial energy density and pressure, respectively.  $\rho_\Lambda$ ,  $\varepsilon_\Lambda$  and  $p_\Lambda$  are determined by ideal-gas relations in terms of temperature, baryon and strange chemical potentials because the system is described by the ideal-gas EoS at the freeze-out stage.

These are the final expressions with which simulations are performed. The feed-down from higher-lying resonances is also taken into account, as it is described in Ref. [13] in detail.

### III. LOCAL EQUILIBRIUM

In addition to the thermal vorticity (12) and meson-field (13) terms, there are other contributions to the spin polarization vector in the local equilibrium [2, 19–22]. These are so-called shear-induced polarization (SIP)

$$S_\mu^{\text{SIP}}(x, p) = \frac{1}{4m_\Lambda} \frac{p^\nu u^\beta p_\rho}{(u \cdot p)} \epsilon_{\mu\nu\alpha\beta} \xi^{\rho\alpha} \quad (15)$$

and polarization induced by the spin-Hall effect (SHE)

$$S_\mu^{\text{SHE}}(x, p) = \frac{1}{4m_\Lambda} \frac{p^\alpha u^\beta}{(u \cdot p)} \epsilon_{\mu\nu\alpha\beta} \partial^\nu \frac{\mu}{T}, \quad (16)$$

where

$$\xi_{\mu\nu} = \frac{1}{2} (\partial_\mu \beta_\nu + \partial_\nu \beta_\mu) \quad (17)$$

is the *thermal shear tensor*, defined as the symmetric derivative of the four-temperature, and  $\mu$  is the chemical potential. These new terms, SIP and SHE, are related to the motion of the particle in anisotropic fluid. They become identically zero in the global equilibrium. To be precise, the above expressions are presented in the explicitly covariant form of Refs. [20, 21], which results from quantum kinetic theory.

As mentioned above, the polarization of the  $\Lambda$  hyperon is measured in its rest frame, see Eq. (9). Therefore, we need the mean spin vector in the  $\Lambda$  rest frame,  $S^{*\mu}$ . In the  $\Lambda$  rest frame the zeroth component  $S^{*0}$  is identically zero and the spatial component becomes

$$\mathbf{S}^*(x, p) = \mathbf{S} - \frac{S^0}{p^0 + m_\Lambda} \mathbf{p} \stackrel{\text{def}}{=} \mathbf{S} - \Delta \mathbf{S} \quad (18)$$

where relation  $\mathbf{p} \cdot \mathbf{S} = p^0 S^0$  was used to modify the conventional expression for  $S^{*\mu}$ . Here,  $p = (p^0, \mathbf{p})$  is the four-momentum of the emitted  $\Lambda$  hyperon and  $S_\mu = S_\mu^\varpi + S_\mu^V + S_\mu^{\text{SIP}} + S_\mu^{\text{SHE}}$  is the mean spin vector that now contains all the relevant terms in the frame of observation.

As aforementioned, the the mean spin vector in the  $\Lambda$  rest frame,  $S^{*\mu}/S_\Lambda$ , should be averaged over the freeze-out hypersurface and particle momenta in order to calculate the global polarization, see Eq. (10). The thermal-vorticity and meson-field contributions are presented in Eqs. (12) and (13). The momentum integration of  $\mathbf{S}^{\text{SIP}}$  and  $\mathbf{S}^{\text{SHE}}$  gives zero [28]

$$\int \frac{d^3p}{p^0} \int d\Sigma^\lambda p_\lambda f_\Lambda S_\mu^{\text{SIP}} = 0, \quad (19)$$

$$\int \frac{d^3p}{p^0} \int d\Sigma^\lambda p_\lambda f_\Lambda S_\mu^{\text{SHE}} = 0. \quad (20)$$

A nonzero result may be produced by finite momentum acceptance.

The corresponding boost corrections  $\Delta \mathbf{S}^{\text{SIP}}$  and  $\Delta \mathbf{S}^{\text{SHE}}$  give nonzero results but they contain additional smallness  $|\mathbf{p}|/(p^0 + m_\Lambda)$ . This is really small parameter in midrapidity, of the order of  $\sim T/m_\Lambda$ . At  $y \approx 1$  it is  $\approx 0.3$  and tends to 1 at  $y \gg 1$ . We approximately put  $1/(p^0 + m_\Lambda) \approx 1/[m_\Lambda(u^0 + 1)]$ . The accuracy of this approximation is  $\sim T/m_\Lambda$ . With this replacement we can immediately perform the momentum integration and arrive at the  $\Delta \mathbf{S}^{\text{SIP}}$  and  $\Delta \mathbf{S}^{\text{SHE}}$  contributions to  $P_\Lambda$ :

$$P_\Lambda^{\text{SIP}} \simeq -\frac{1}{2m_\Lambda} \int_{\Sigma_{\Delta y}} d^3x \frac{u^0 p_\Lambda}{(u^0 + 1)} \Xi_{zx} / \int d^3x \rho_\Lambda, \quad (21)$$

$$P_\Lambda^{\text{SHE}} \simeq \frac{1}{m_\Lambda^2} \int_{\Sigma_{\Delta y}} d^3x \frac{u^0 p_\Lambda}{(u^0 + 1)} \zeta_{zx} / \int d^3x \rho_\Lambda, \quad (22)$$

where

$$\Xi_{\mu\nu} = u_\mu u^\lambda \xi_{\nu\lambda} - u_\nu u^\lambda \xi_{\mu\lambda}, \quad (23)$$

$$\zeta_{\mu\nu} = \frac{1}{2} \left( u_\mu \partial_\nu \frac{\mu}{T} - u_\nu \partial_\mu \frac{\mu}{T} \right), \quad (24)$$

and  $p_\Lambda$  is the partial pressure of  $\Lambda$  hyperons, see Eq. (14). The chemical potential is  $\mu = B\mu_B + S\mu_S$ , where  $\mu_B$  and  $\mu_S$  are baryon and strangeness chemical potentials, respectively,  $B$  and  $S$  are baryon and strangeness charges of the considered baryon. For  $\Lambda$  hyperon  $\mu = \mu_B - \mu_S$ . Here  $d^3x$  integration runs over cells, where condition  $|y_h| < y_{\text{acceptance}}$  is met. This part the hypersurface is denoted as  $\Sigma_{\Delta y}$ , similarly to that in Eqs. (12) and (13).

If we divide the thermal-shear vorticity (23) into kinematic part,  $\tilde{\Xi}_{\mu\nu}$ , and the part due to  $T$  derivatives, similarly to that in Eq. (2),

$$\Xi_{\mu\nu} = \tilde{\Xi}_{\mu\nu} + \omega_{\mu\nu}^{(T)}, \quad (25)$$

$$\tilde{\Xi}_{\mu\nu} = \frac{1}{2T} [u_\mu(u^\lambda \partial_\lambda)u_\nu - u_\nu(u^\lambda \partial_\lambda)u_\mu], \quad (26)$$

we see that the part of  $\Xi_{\mu\nu}$  due to  $T$  derivatives is precisely the same as that in the thermal vorticity (4). It does not mean that their contributions to the global polarization are equal because they are integrated with different weights over the freeze-out hypersurface.

Comparing expressions (21) and (22) with that for the thermal vorticity (12), we see that the SIP and SHE contributions indeed contain additional smallness  $u^0 p_\Lambda / \rho_\Lambda \sim T/m_\Lambda$  compared to  $P_\Lambda^\varpi$ , as it was mentioned above.

#### IV. RESULTS

The global  $\Lambda$  polarization in Au+Au collisions is considered in the energy range  $3 \leq \sqrt{s_{NN}} \leq 9$  GeV, which is relevant to the STAR-FXT experiment and upcoming BM@N and MPD experiments at NICA. This energy range has been already studied in Ref. [13]. Here a more systematic study is presented. Special attention is paid to the collision energies of  $\sqrt{s_{NN}} = 3.2, 3.5, 3.9$ , and 4.5 GeV. The corresponding results can be considered as predictions for the STAR-FXT experimental data that are expected in the nearest future.

The simulations closely follow the procedure described in Ref. [13]. They are performed within the 3FD model [23, 24] combined with thermodynamic approach to the particle polarization [25–27] supplemented by the meson-field induced contribution [14], as well as the SIP and SHE contributions [20, 21] that are present in the local equilibrium. All results presented below are calculated taking into account feed-down from higher-lying resonances, based on prescription of Ref. [13]. The feed-down reduces  $P_\Lambda$  by  $\approx 20\%$  at considered collision energies.

The simulations are performed at fixed impact parameters, see Tab. I. To associate these impact parameters with collision centrality, one should keep in mind that in the 3FD model the colliding nuclei have a shape of sharp spheres without the Woods-Saxon diffuse edge. This fact, implemented in the Glauber simulations based on the

nuclear overlap calculator [31], results in sharp-edge centralities being  $\approx 1.4$  larger than those for diffuse-edge case at the same impact parameter, see Tab. I. This way

b(fm)	“sharp-edge” centrality*	“diffuse-edge” centrality
2	2.5%	1.8%
4	10%	7%
6	23%	16.5%
8	41%	29%

TABLE I: Impact parameters of Au+Au collisions and corresponding centralities calculated by means of the Glauber simulations (the nuclear overlap calculator [31]) for two cases: the colliding nuclei have a “sharp-edge” and “diffuse-edge” shape. \* “Sharp-edge” nuclei are used in present simulations.

of association of impact parameters with experimental centrality was successfully applied in previous studies of global polarization [8, 13], light-(hyper)nuclei production [32–34] and directed flow [35] in the considered energy range.

The physical input of the present 3FD calculations is described in Ref. [24]. The simulations are done with two equations of state (EoS’s) with the deconfinement transitions [36], i.e. a first-order phase transition (1PT) and a crossover one. These EoS’s give very similar predictions at  $\sqrt{s_{NN}} < 4$  GeV [32–35]. However, 1PT and crossover results become differ at  $\sqrt{s_{NN}} > 4$  GeV, especially for the directed flow [35].

The thermodynamic approach to the particle polarization [19, 22, 25–27] is based on the assumption of local thermal equilibrium that is not evident at moderately relativistic energies because the collision dynamics becomes less equilibrium with the collision energy decrease. Nevertheless, it was found that the equilibrium is achieved at the freeze-out stage [13, 37, 38]. The success of the statistical model [39] at moderate energies also indicates the thermalization at the freeze-out.

##### A. Collision Energy Dependence

The global  $\Lambda$  polarization in midrapidity regions  $|y_h| < 0.8$  in Au+Au collisions at different impact parameters ( $b$ ) as function of collision energy  $\sqrt{s_{NN}}$  is presented in Fig. 1. Available data from Refs. [3, 11, 18] (STAR) and [12] (HADES) are also demonstrated. These data were obtained in measurements with different acceptances, see Tab. II. The simulations with  $b = 6$ –8 fm and  $|y_h| < 0.8$  (or  $|y_h| < 0.6$  for HADES [12]) most closely match these acceptance conditions, with the caveat that  $y_h$  is the hydrodynamic rapidity, not the true one. These symmetric windows are not that good for the low-energy data [11, 12, 18], where rapidity acceptance is asymmetric with respect to the midrapidity. However, it is still suitable in view of quite flat rapidity dependence of the observed  $P_\Lambda$ .

$\sqrt{s_{NN}}$ (GeV)	exp. centrality	$b$ (fm)	(pseudo)rapidity
2.4 [12]	20–40%	6–8	$-0.5 < y < 0.3$
3 [11]	20–50%	6–9	$-0.2 < y < 1$
7.2 [18]	20–60%	6–10	$-1.5 < \eta < 0$
7.7 [3]	20–50%	6–9	$ \eta  < 1$

TABLE II: Acceptances of data available at collision energies of  $2.4 \leq \sqrt{s_{NN}} \leq 7.7$  GeV: [3, 11, 18] (STAR) and [12] (HADES). Experimental centralities are associated with impact parameters of Au+Au collisions by means of the Glauber simulations [31] for colliding “sharp-edge” nuclei.

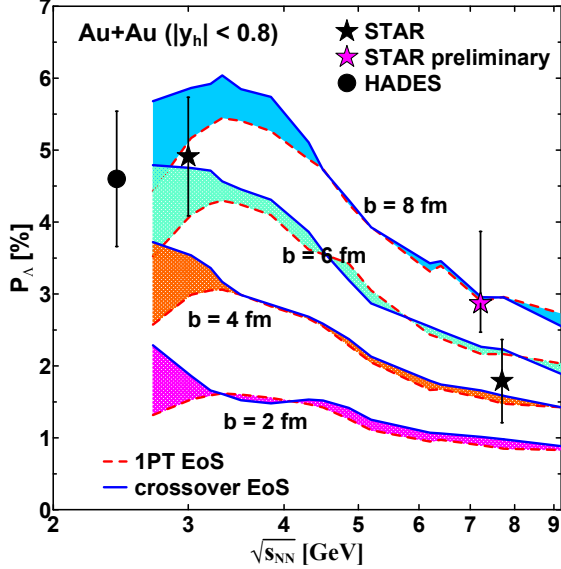


FIG. 1: Global  $\Lambda$  polarization in midrapidity region  $|y_h| < 0.8$  in Au+Au collisions at different impact parameters ( $b$ ) as function of collision energy  $\sqrt{s_{NN}}$ . Results for different EoS’s are presented. Areas between results for different EoS’s at the same  $b$  are shaded. Data are from Refs. [3, 11, 18] (STAR) and [12] (HADES).

As seen from Fig. 1, results that are obtained with 1PT and crossover EoS’s are very close except for the region of low collision energies  $\sqrt{s_{NN}} \leq 3$  GeV, where they start to diverge. At the same time all other observables, bulk and flow ones, are either identical or very similar within the 1PT and crossover scenarios at  $\sqrt{s_{NN}} \leq 3$  GeV [24, 32–35, 40, 41] because the 1PT and crossover EoS’s are very similar in the corresponding range of the phase diagram. Therefore, the diverge of  $P_\Lambda$  predicted by the 1PT and crossover scenarios indicates enhanced numerical fluctuations in derivative computation at low collision energies. This is why we avoid doing  $P_\Lambda$  predictions for  $\sqrt{s_{NN}} < 3$  GeV. Here and below, the areas between corresponding results for different EoS’s are shaded in order to visualize the accuracy of the calculation.

The calculation shows that a broad maximum of  $P_\Lambda$  is reached at  $\sqrt{s_{NN}} \approx 3$ –3.5 GeV at  $b = 8$  fm and proba-

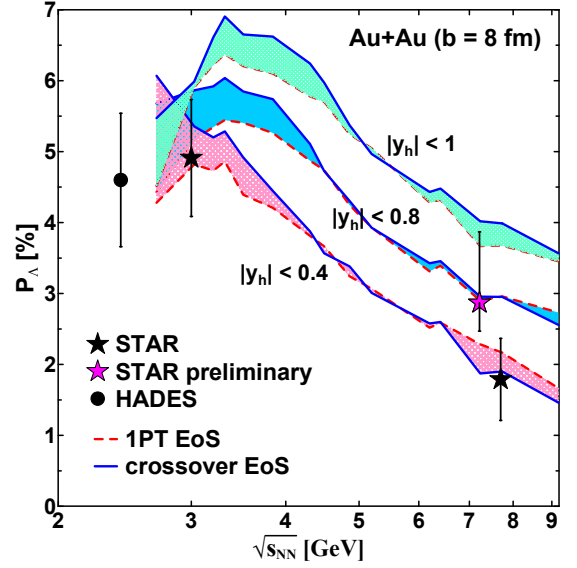


FIG. 2: Global  $\Lambda$  polarization in different midrapidity regions  $|y_h|$  in Au+Au collisions at  $b = 8$  fm as function of collision energy  $\sqrt{s_{NN}}$ . Results for different EoS’s are presented. Areas between results for different EoS’s at the same  $|y_h|$  are shaded. Data are from Refs. [3, 11, 18] (STAR) and [12] (HADES).

bly at lower  $\sqrt{s_{NN}}$  at smaller  $b$ . The  $P_\Lambda$  increases with rising  $b$  because of increase of the angular momentum accumulated in the participant matter.

The global  $\Lambda$  polarization in different midrapidity regions  $|y_h|$  in Au+Au collisions at  $b = 8$  fm as function of collision energy  $\sqrt{s_{NN}}$  is displayed in Fig. 2. The maximum of  $P_\Lambda$  between 3.2 and 3.9 GeV becomes more pronounced at  $|y_h| < 1$ . It moves to lower energies in narrower rapidity windows.

## B. Rapidity dependence

The fixed-target measurements [11, 12] also give information on the rapidity dependence of the global polarization. The first predictions of the rapidity dependence of  $P_\Lambda$  in experiments within STAR-FXT program were made in Ref. [9] within A Multi-Phase Transport (AMPT) model [42, 43]. Although these predictions do not quantitatively agree with the STAR-FXT data at 3 GeV [11], it is instructive to qualitatively consider them. While the global polarization reveals quite strong increase from the midrapidity to forward/backward rapidities at  $5 \text{ GeV} \leq \sqrt{s_{NN}} \leq 27 \text{ GeV}$ , at  $\sqrt{s_{NN}} = 3 \text{ GeV}$  it turns to decrease from the midrapidity to peripheral rapidities, whereas the experimental dependence is quite flat at both 3 [11] and 7.2 GeV [18]. At the same time, simulations within the 3FD model result in polarization increase from the midrapidity to forward/backward rapidities, in contrast to that in the AMPT model. This is a consequence of different vortex dynamics within the

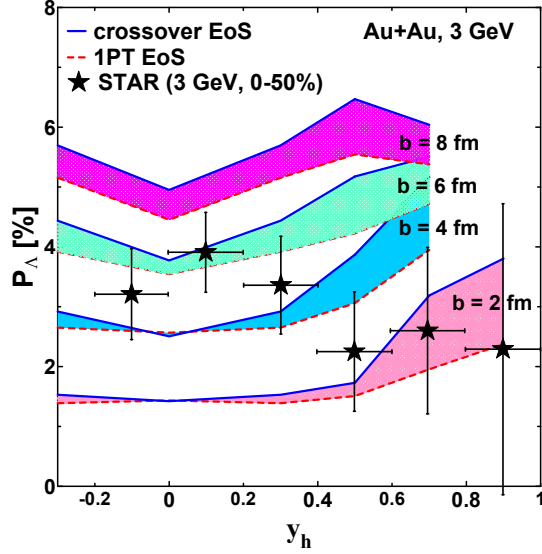


FIG. 3: Rapidity dependence of the global  $\Lambda$  polarization in Au+Au collisions at  $\sqrt{s_{NN}} = 3$  GeV and different centralities (impact parameters  $b$ ). Results for different EoS's are presented. Areas between results for different EoS's at the same  $b$  are shaded. Data from Ref. [11] (STAR) correspond to centrality 0–50%, i.e.  $b = 0$ –9 fm.

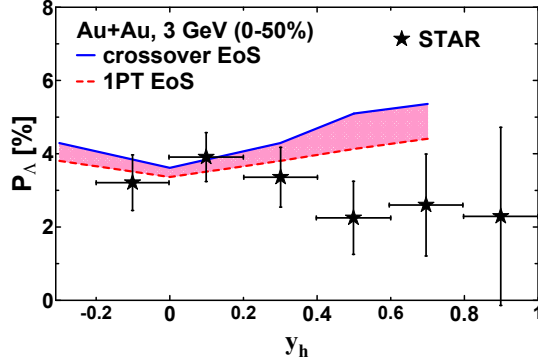


FIG. 4: Rapidity dependence of the global  $\Lambda$  polarization in Au+Au collisions at  $\sqrt{s_{NN}} = 3$  GeV and centrality 0–50%. Results for different EoS's are presented. Data are from Ref. [11] (STAR).

AMPT and 3FD models. In the 3FD model, the vorticity is mainly located at the border between participants and spectators [44], which results in rise of  $P_\Lambda$  from the midrapidity to forward/backward rapidities. In particular, it may result in formation of so-called vortex rings [45–49].

The calculated rapidity dependence of  $P_\Lambda$  in Au+Au collisions at  $\sqrt{s_{NN}} = 3$  GeV at different impact parameters  $b$  (i.e., centralities, see Tab. I) is presented in Fig. 3. Again, the shaded areas between results for different EoS's demonstrate the accuracy of the calculation. Results for larger impact parameters ( $b \geq 4$  fm) are displayed only up to  $y_h = 0.7$  because the calcula-

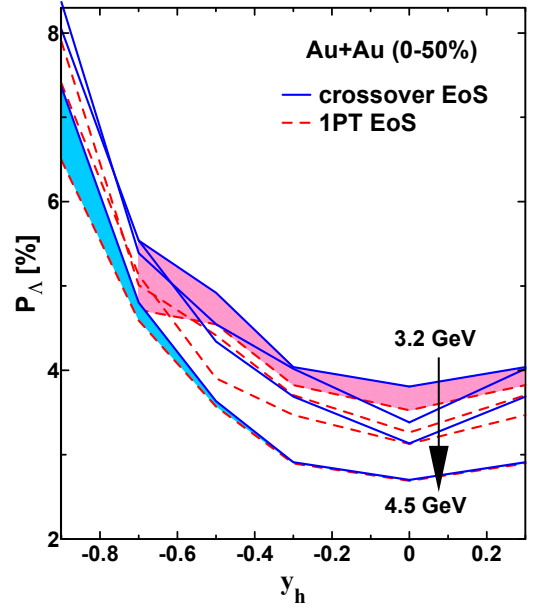


FIG. 5: The same as in Fig. 4 but for  $\sqrt{s_{NN}} = 3.2, 3.5, 3.9$ , and 4.5 GeV. Areas between results for different EoS's at energies of 3.2 and 4.5 GeV are shaded.

tion accuracy becomes poor at  $y_h > 0.7$ . The presented STAR [11] data correspond to centrality of 0–50%, i.e.  $b = 0$ –9 fm, see table II, which makes it difficult to draw conclusions about the degree of reproduction of the data because such a wide range of impact parameters cannot be represented by a single impact parameter. Therefore, we need to perform averaging over  $b$ :

$$\langle P_\Lambda \rangle = \int_0^{b_{max}} b db P_\Lambda(b) / \int_0^{b_{max}} b db \quad (27)$$

where  $b_{max} = 9$  fm. Actual 3FD simulations of Au+Au collisions were performed at discrete impact parameters  $b = 2, 4, 6$ , and 8 fm. Therefore, we replace the integral in Eq. (27) by a sum over impact parameters

$$\langle P_\Lambda \rangle \approx \sum_{b_i=2,4,6,8\text{fm}} b_i P_\Lambda(b_i) / \sum_{b_i=2,4,6,8\text{fm}} b_i, \quad (28)$$

where  $\Delta b$  is canceled because  $b_i$  points are equidistant.

The rapidity dependence of the global  $\Lambda$  polarization at  $\sqrt{s_{NN}} = 3$  GeV, calculated accordingly to Eq. (28), is shown in Fig. 4. This calculation well reproduces the experimental rapidity dependence in the midrapidity range ( $|y_h| \leq 0.3$ ), while it overestimates the data at forward rapidities. Predictions of the rapidity dependence of  $P_\Lambda$  in Au+Au collisions at  $\sqrt{s_{NN}} = 3.2, 3.5, 3.9$ , and 4.5 GeV in centrality range of 0–50% are displayed in Fig. 5. The shapes of the rapidity distributions at 3.5, 3.9, and 4.5 GeV turn out to be very similar (up to numerical uncertainties). Only the overall normalization decreases with the collision energy increase. It is difficult to draw conclusions about this shape at 3.2 GeV due to high numerical uncertainties.

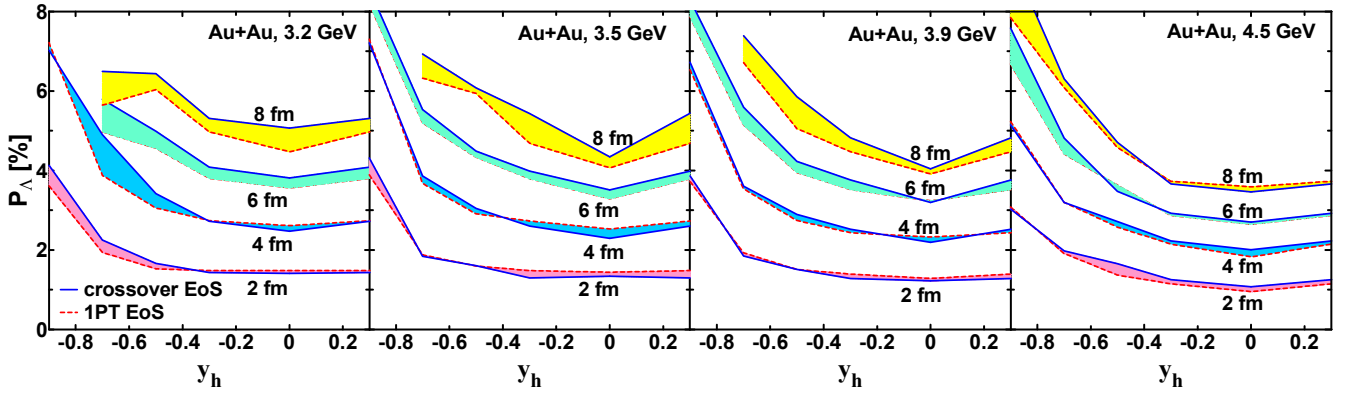


FIG. 6: The same as in Fig. 3 but for  $\sqrt{s_{NN}} = 3.2, 3.5, 3.9$ , and  $4.5$  GeV.

The predicted rapidity dependence of  $P_\Lambda$  in Au+Au collisions at  $\sqrt{s_{NN}} = 3.2, 3.5, 3.9$ , and  $4.5$  GeV at different impact parameters  $b$  is presented in Fig. 6. Again, results for larger impact parameters are displayed only up to  $|y_h| = 0.7$  because of poor accuracy at  $|y_h| > 0.7$ . The  $P_\Lambda$  increases in the forward/backward rapidities, which implies that larger gradients need to be considered. Numerical evaluation of these large gradients on the grid results in a loss of accuracy. Also  $P_\Lambda$  (and hence the spacial gradients) increases with  $b$  rise. As a result, numerical accuracy is noticeably worse at  $b = 8$  fm than that at 2 fm.

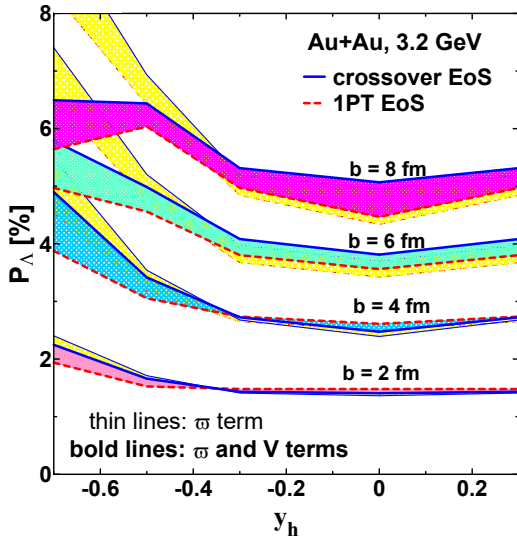


FIG. 7: Rapidity dependence of the global  $\Lambda$  polarization in Au+Au collisions at  $\sqrt{s_{NN}} = 3.2$  GeV and different impact parameters  $b$  with (bold lines) and without (thin lines) the meson-field contribution. Results for different EoS's are presented.

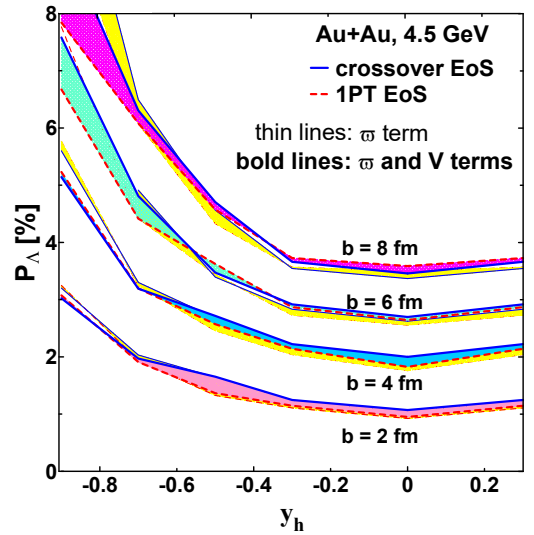


FIG. 8: The same as in Fig. 7 but for  $\sqrt{s_{NN}} = 4.5$  GeV.

### C. Meson-Field Contribution

The impact of the meson-field contribution to the  $P_\Lambda$ , Eq. 6, was studied in detail in Ref. [13] at the examples of collisions at energies of  $\sqrt{s_{NN}} = 3$  and  $7.7$  GeV. It was found that the meson-field contribution considerably flattens the rapidity distributions, which otherwise are strongly forward/backward peaked when only the thermal vorticity is taken into account. It improves agreement of calculated polarization with available data at 3 and  $7.7$  GeV. At the same time, the meson-field contribution is practically negligible at the midrapidity. Note that one of many possible parametrizations of the meson-field interaction was used in the present and former [13] calculations. It indicates the order of magnitude and character of the produced effect. The details may be different for other, more refined parametrizations, e.g., such as those developed in Refs. [50–52] for astrophysical applications.



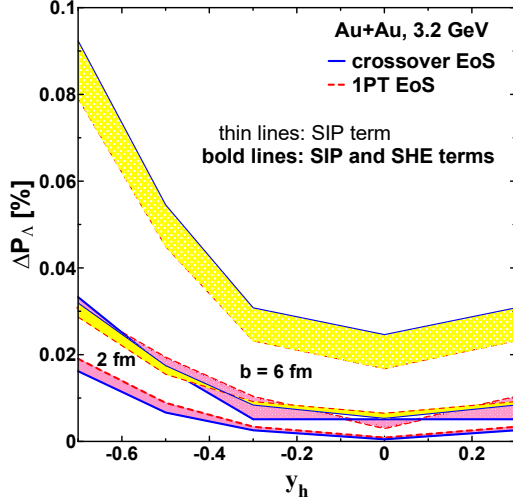


FIG. 9: Rapidity dependence of the SIP (thin lines) and SIP+SHE (bold lines) contributions to  $P_\Lambda$  in Au+Au collisions at  $\sqrt{s_{NN}} = 3.2$  GeV and different impact parameters  $b$ . Results for different EoS's are presented.

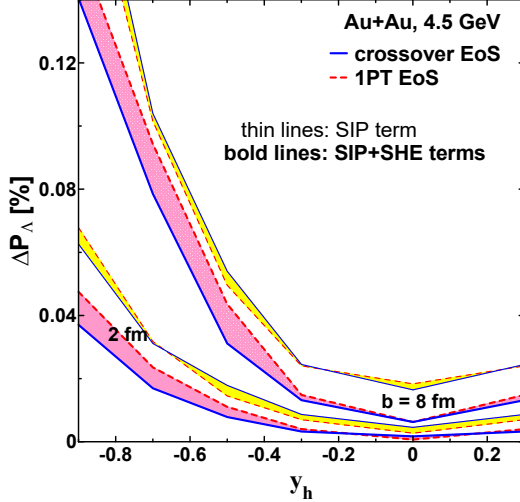


FIG. 10: The same as in Fig. 9 but for  $\sqrt{s_{NN}} = 4.5$  GeV.

Here, the effect of the meson-field contribution is demonstrated for the Au+Au collisions at energies that are considered in this paper, see Figs. 7 and 8. These figures demonstrate the same features as before: the meson-field contribution considerably reduces  $P_\Lambda$  at backward rapidities in semicentral collisions ( $b = 6$  and  $8$  fm) at  $\sqrt{s_{NN}} = 3.2$  GeV, see Figs. 7. The polarization remains practically unchanged in central collisions. The influence of the meson-field contribution reduces with the  $\sqrt{s_{NN}}$  rise. At  $4.5$  GeV,  $P_\Lambda$  even at backward rapidities in semicentral collisions is only slightly affected by this contribution.

#### D. SIP and SHE Contributions

As aforementioned in sect. III, the SIP and SHE contributions, see Eqs. (21) and (22), have additional smallness  $\sim T/m_\Lambda$  compared to that due to thermal vorticity (12). Authors of Refs. [53, 54] found that the SIP and SHE contributions to the global polarization are insignificant at the collision energies of  $7.7$ – $27$  GeV. In this subsection, the SIP and SHE effects in the in the FXT-STAR energy range are demonstrated.

The results of the calculations are presented in Figs 9 and 10. As seen, the SIP and SHE contributions are negligible as compared with thermal-vorticity polarization. Moreover, the SIP and SHE contributions partially cancel each other. This calculation is stronger at  $3.2$  GeV.

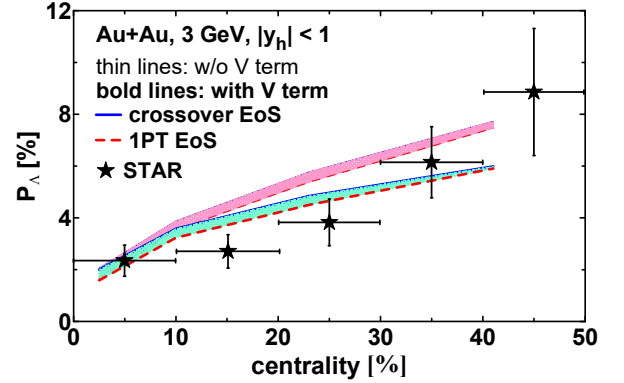


FIG. 11: Centrality dependence of the global  $\Lambda$  polarization in Au+Au collisions at  $\sqrt{s_{NN}} = 3$  GeV in rapidity window  $y_h \leq 1$ . with (bold lines) and without (thin lines) the meson-field contribution (V) Results for different EoS's are presented. Areas between results for different EoS's at the same  $b$  are shaded. Data are from Ref. [11].

#### E. Centrality Dependence

Centrality dependence of  $P_\Lambda$  in Au+Au collisions at  $\sqrt{s_{NN}} = 3$  GeV in rapidity window  $y_h \leq 1$  is presented in Fig. 11 and compared with STAR data [11]. Correspondence between impact parameters and centralities is taken from Tab. I. Results with and without the meson-field contribution, Eq. 6, are presented. The meson-field corrections is sizable in semicentral collisions, as it has been already pointed out in subsect. IVC, see Fig. 7. However, it is difficult to draw conclusions on its relevance because of large error bars of the data. The obtained results are in good agreement with the STAR data in very central (3–10% centrality) and semi-peripheral (30–40% centrality) collisions while overestimate the data at centralities of 10–30%.

Predictions of the centrality dependence of  $P_\Lambda$  in Au+Au collisions at  $\sqrt{s_{NN}} = 3.2, 3.5, 3.9$ , and  $4.5$  GeV are displayed in Fig. 12. The STAR data [11] for  $\sqrt{s_{NN}} = 3$  GeV are kept in this figure as reference



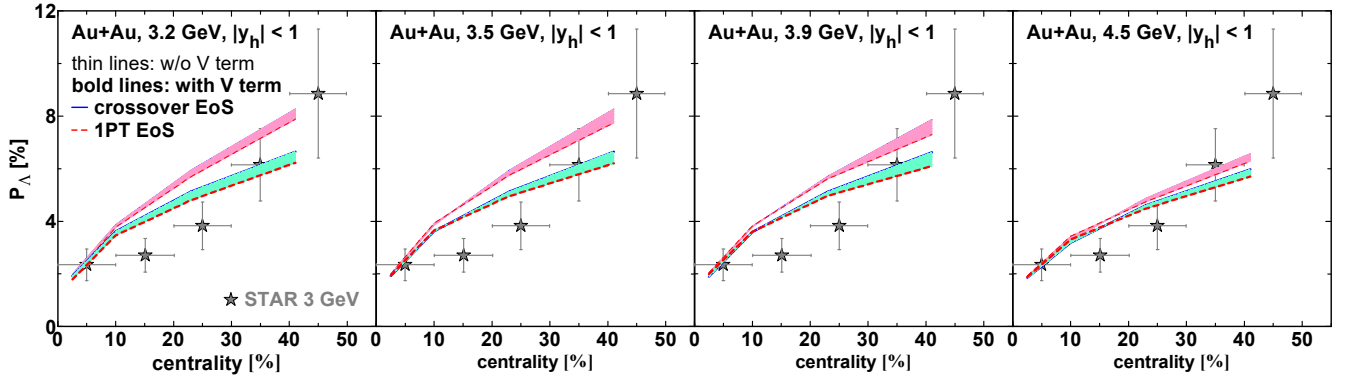


FIG. 12: The same as in Fig. 11 but for  $\sqrt{s_{NN}} = 3.2, 3.5, 3.9$ , and  $4.5$  GeV. Data for  $\sqrt{s_{NN}} = 3$  GeV [11] are displayed to provide reference points for comparison.

points for comparing results at different collision energies. The meson-field corrections become smaller with the collision energy rise. The centrality dependences (with the  $V$  term) at 3.2, 3.5, and 3.9 GeV are practically identical. At and 4.5 GeV, the  $P_\Lambda$  the overall drop of  $P_\Lambda$  starts. Notice that the maximum of  $P_\Lambda$  is reached at 3.2–3.5 GeV if meson-field corrections are disregarded.

## V. SUMMARY

Based on the 3FD model, the global  $\Lambda$  polarization in Au+Au collisions at moderately relativistic energies  $3 \leq \sqrt{s_{NN}} \leq 9$  GeV was studied. Various contributions to the global polarization were considered. These are contributions due to the thermal vorticity, meson field [14], thermal shear and spin-Hall effect [20, 21]. Feed-down from higher-lying resonances was also taken into account, which, as found, reduces the polarization by  $\approx 20\%$ . The results were compared with available data [11, 12, 18]. These simulations closely followed the procedure described in Ref. [13].

Special attention was paid to the collision energies of  $\sqrt{s_{NN}} = 3, 3.2, 3.5, 3.9$ , and  $4.5$  GeV, for which a thorough scan of the rapidity and centrality dependence of the global  $\Lambda$  polarization was performed. The results for 3 GeV reasonably well reproduced the corresponding STAR data [11]. While the corresponding results at  $\sqrt{s_{NN}} = 3.2, 3.5, 3.9$ , and  $4.5$  GeV can be considered as predictions for the STAR-FXT experimental data that are expected in the nearest future. They are also relevant to forthcoming experiments at NICA.

The simulations were performed with two equations of state with the deconfinement transition [36], i.e. a first-order phase transition (1PT) and a crossover one. Results that are obtained with 1PT and crossover EoS's are very close except for the region of low collision energies  $\sqrt{s_{NN}} \leq 3$  GeV, where they start to diverge. At the same time all other observables, bulk and flow ones, are either identical or very similar within the 1PT and crossover scenarios at  $\sqrt{s_{NN}} \leq 3$  GeV [24, 32–35, 40, 41]

because these EoS's are very similar in the corresponding range of the phase diagram. Therefore, the diverge of  $P_\Lambda$  predicted by the 1PT and crossover scenarios indicates enhanced numerical fluctuations in derivative computation at low collision energies. This is why we avoided doing  $P_\Lambda$  predictions for  $\sqrt{s_{NN}} < 3$  GeV.

The global polarization increases with the collision energy decrease. It was predicted that a broad maximum of  $P_\Lambda$  is reached at  $\sqrt{s_{NN}} \approx 3$ – $3.9$  GeV depending on the width of the midrapidity range of observation. The maximum of  $P_\Lambda$  between 3.2 and 3.9 GeV becomes more pronounced in the midrapidity window  $|y| < 1$ . It moves to lower energies in narrower rapidity windows and smaller impact parameters. The  $P_\Lambda$  increases with increasing impact parameter because of increase of the angular momentum accumulated in the participant matter.

It was found that the meson-field contribution considerably reduces  $P_\Lambda$  at forward/backward rapidities in semicentral collisions at  $3 \leq \sqrt{s_{NN}} \leq 3.9$  GeV. The polarization remains practically unchanged in central collisions. The influence of the meson-field contribution reduces with the  $\sqrt{s_{NN}}$  rise. At 4.5 GeV,  $P_\Lambda$  even at forward/backward rapidities in semicentral collisions is only slightly affected by this contribution. The results of the calculations showed that the SIP and SHE contributions are negligible as compared with thermal-vorticity polarization. Moreover, the SIP and SHE contributions partially cancel each other.

All the above results were obtained in terms of hydrodynamic rapidities, see Eq. (11), rather than true rapidities of observed particles. In addition, the momentum-integrated global polarization was calculated, which does not take into account the transverse-momentum acceptance. All this implies a semi-quantitative description of the experimental data.

In recent paper [55], it was suggested that the global polarization correlates with the baryon stopping in nuclear collisions. The stronger counter-streaming baryons interact with each other, the more vortical collective flow they produce. The baryon stopping is indeed stronger at lower collision energies, which may explain the increase

of the global polarization with decreasing collision energy. However, it is difficult to experimentally quantify the baryon stopping. Even at the complete stopping, the proton rapidity distribution in high-energy collisions has a dip in the midrapidity because of almost one-dimensional hydrodynamical expansion of the produced nuclear matter [56, 57]. This fact was noticed long ago by L.D. Landau in his hydrodynamical theory of multiple production of particles [58]. This rapidity distribution is qualitatively the same as that resulting from incomplete baryon stopping. At the same time, the directed flow is strongly affected by the baryon stopping. The directed flow is a well-defined observable. Moreover, the correlation between the global polarization and directed flow

was predicted in Refs. [59–62]. This correlation is well measurable and may, in particular, indirectly reflect the correlation between the global polarization and baryon stopping.

## Acknowledgments

This work was carried out using computing resources of the federal collective usage center “Complex for simulation and data processing for mega-science facilities” at NRC “Kurchatov Institute” [63].

- 
- [1] T. Niida and S. A. Voloshin, Polarization phenomenon in heavy-ion collisions, *Int. J. Mod. Phys. E* **33**, no.09, 2430010 (2024) [arXiv:2404.11042 [nucl-ex]].
  - [2] F. Becattini, M. Buzzegoli, T. Niida, S. Pu, A. H. Tang and Q. Wang, Spin polarization in relativistic heavy-ion collisions, *Int. J. Mod. Phys. E* **33**, no.06, 2430006 (2024) [arXiv:2402.04540 [nucl-th]].
  - [3] L. Adamczyk *et al.* [STAR Collaboration], Global  $\Lambda$  hyperon polarization in nuclear collisions: evidence for the most vortical fluid, *Nature* **548**, 62 (2017) [arXiv:1701.06657 [nucl-ex]].
  - [4] J. Adam *et al.* [STAR Collaboration], Global polarization of  $\Lambda$  hyperons in Au+Au collisions at  $\sqrt{s_{NN}} = 200$  GeV, *Phys. Rev. C* **98**, 014910 (2018) [arXiv:1805.04400 [nucl-ex]].
  - [5] X. G. Deng, X. G. Huang, Y. G. Ma and S. Zhang, Vorticity in low-energy heavy-ion collisions, *Phys. Rev. C* **101**, no.6, 064908 (2020) [arXiv:2001.01371 [nucl-th]].
  - [6] Y. B. Ivanov, V. D. Toneev and A. A. Soldatov, Estimates of hyperon polarization in heavy-ion collisions at collision energies  $\sqrt{s_{NN}} = 4\text{--}40$  GeV, *Phys. Rev. C* **100**, no. 1, 014908 (2019) [arXiv:1903.05455 [nucl-th]].
  - [7] Y. B. Ivanov, V. D. Toneev and A. A. Soldatov, Vorticity and Particle Polarization in Relativistic Heavy-Ion Collisions, *Phys. Atom. Nucl.* **83**, no. 2, 179 (2020). [arXiv:1910.01332 [nucl-th]].
  - [8] Y. B. Ivanov, Global  $\Lambda$  polarization in moderately relativistic nuclear collisions, *Phys. Rev. C* **103**, no.3, L031903 (2021) [arXiv:2012.07597 [nucl-th]].
  - [9] Y. Guo, J. Liao, E. Wang, H. Xing and H. Zhang, Hyperon polarization from the vortical fluid in low-energy nuclear collisions, *Phys. Rev. C* **104**, no.4, L041902 (2021) [arXiv:2105.13481 [nucl-th]].
  - [10] A. Ayala, I. Domínguez, I. Maldonado and M. E. Tejeda-Yeomans, Rise and fall of  $\Lambda$  and  $\bar{\Lambda}$  global polarization in semi-central heavy-ion collisions at HADES, NICA and RHIC energies from the core-corona model, *Phys. Rev. C* **105**, no.3, 034907 (2022) [arXiv:2106.14379 [hep-ph]].
  - [11] M. S. Abdallah *et al.* [STAR], Global  $\Lambda$ -hyperon polarization in Au+Au collisions at  $\sqrt{s_{NN}}=3$  GeV, *Phys. Rev. C* **104**, no.6, L061901 (2021) [arXiv:2108.00044 [nucl-ex]].
  - [12] R. Abou Yassine *et al.* [HADES], Measurement of global polarization of  $\Lambda$  hyperons in few-GeV heavy-ion collisions, *Phys. Lett. B* **835**, 137506 (2022) [arXiv:2207.05160 [nucl-ex]].
  - [13] Y. B. Ivanov and A. A. Soldatov, Global  $\Lambda$  polarization in heavy-ion collisions at energies 2.4–7.7 GeV: Effect of meson-field interaction, *Phys. Rev. C* **105**, no.3, 034915 (2022) [arXiv:2201.04527 [nucl-th]].
  - [14] L. Csernai, J. Kapusta and T. Welle,  $\Lambda$  and  $\bar{\Lambda}$  spin interaction with meson fields generated by the baryon current in high energy nuclear collisions, *Phys. Rev. C* **99**, no.2, 021901 (2019) [arXiv:1807.11521 [nucl-th]].
  - [15] Y. Xie, G. Chen and L. P. Csernai, A study of  $\Lambda$  and  $\bar{\Lambda}$  polarization splitting by meson field in PICR hydrodynamic model, *Eur. Phys. J. C* **81**, no.1, 12 (2021) [arXiv:1912.00209 [hep-ph]].
  - [16] B. D. Serot and J. D. Walecka, *Int. J. Mod. Phys. E* **06**, 515 (1997).
  - [17] J. Cohen and H. J. Weber, Relativistic sigma - omega mean field theory for hyperons from a quark model, *Phys. Rev. C* **44**, 1181 (1991).
  - [18] K. Okubo [STAR], Measurement of global polarization of  $\Lambda$  hyperons in Au+Au  $\sqrt{s_{NN}} = 7.2$  GeV fixed target collisions at RHIC-STAR experiment, *EPJ Web Conf.* **259**, 06003 (2022) [arXiv:2108.10012 [nucl-ex]].
  - [19] F. Becattini, M. Buzzegoli and A. Palermo, Spin-thermal shear coupling in a relativistic fluid, *Phys. Lett. B* **820**, 136519 (2021) [arXiv:2103.10917 [nucl-th]].
  - [20] S. Y. F. Liu and Y. Yin, Spin polarization induced by the hydrodynamic gradients, *JHEP* **07**, 188 (2021) [arXiv:2103.09200 [hep-ph]].
  - [21] S. Y. F. Liu and Y. Yin, Spin Hall effect in heavy-ion collisions, *Phys. Rev. D* **104**, no.5, 054043 (2021) [arXiv:2006.12421 [nucl-th]].
  - [22] F. Becattini, M. Buzzegoli, A. Palermo, G. Inghirami and I. Karpenko, Local polarization and isothermal local equilibrium in relativistic heavy ion collisions, [arXiv:2103.14621 [nucl-th]].
  - [23] Yu. B. Ivanov, V. N. Russkikh, and V.D. Toneev, *Phys. Rev. C* **73**, 044904 (2006) [nucl-th/0503088].
  - [24] Yu. B. Ivanov, Alternative Scenarios of Relativistic Heavy-Ion Collisions: I. Baryon Stopping, *Phys. Rev. C* **87**, 064904 (2013) [arXiv:1302.5766 [nucl-th]].
  - [25] F. Becattini, V. Chandra, L. Del Zanna and E. Grossi, Relativistic distribution function for particles with spin at local thermodynamical equilibrium, *Annals Phys.* **338**, 32 (2013) [arXiv:1303.3431 [nucl-th]].

- [26] F. Becattini, I. Karpenko, M. Lisa, I. Uppsal and S. Voloshin, Global hyperon polarization at local thermodynamic equilibrium with vorticity, magnetic field and feed-down, *Phys. Rev. C* **95**, no. 5, 054902 (2017) [arXiv:1610.02506 [nucl-th]].
- [27] R. h. Fang, L. g. Pang, Q. Wang and X. n. Wang, Polarization of massive fermions in a vortical fluid, *Phys. Rev. C* **94**, no. 2, 024904 (2016) [arXiv:1604.04036 [nucl-th]].
- [28] Y. B. Ivanov and A. A. Soldatov, On ambiguity of definition of shear and spin-hall contributions to  $\Lambda$  polarization in heavy-ion collisions, *JETP Lett.* **116**, no.3, 133 (2022) [arXiv:2206.06927 [hep-ph]].
- [29] V. N. Russkikh and Yu. B. Ivanov, Dynamical freeze-out in 3-fluid hydrodynamics, *Phys. Rev. C* **76**, 054907 (2007) [nucl-th/0611094].
- [30] Yu. B. Ivanov and V. N. Russkikh, On freeze-out problem in relativistic hydrodynamics, *Phys. Atom. Nucl.* **72**, 1238 (2009) [arXiv:0810.2262 [nucl-th]].
- [31] <http://web-docs.gsi.de/~misko/overlap/interface.html>
- [32] M. Kozhevnikova and Y. B. Ivanov, Light-nuclei production in Au+Au collisions at  $\sqrt{s_{NN}}=3$  GeV within a thermodynamical approach: Bulk properties and collective flow, *Phys. Rev. C* **109**, no.1, 014913 (2024) [arXiv:2311.08092 [nucl-th]].
- [33] M. Kozhevnikova and Y. B. Ivanov, Production of light hypernuclei in Au+Au collisions at  $\sqrt{s_{NN}}=3$  GeV within a thermodynamic approach, *Phys. Rev. C* **109**, no.3, 034901 (2024) [arXiv:2401.04991 [nucl-th]].
- [34] M. Kozhevnikova and Y. B. Ivanov, Light-Nuclei Production in Heavy-Ion Collisions at  $\sqrt{s_{NN}} = 6.4 - 19.6$  GeV in THESEUS Generator Based on Three-Fluid Dynamics, *Particles* **6**, no.1, 440-450 (2023)
- [35] Y. B. Ivanov and M. Kozhevnikova, Examination of STAR fixed-target data on directed flow at  $\sqrt{s_{NN}}=3$  and 4.5 GeV, *Phys. Rev. C* **110**, no.1, 014907 (2024) [arXiv:2403.02787 [nucl-th]].
- [36] A. S. Khvorostukhin, V. V. Skokov, K. Redlich, and V. D. Toneev, *Eur. Phys. J.* **C48**, 531 (2006) [nucl-th/0605069].
- [37] Y. B. Ivanov and A. A. Soldatov, Equilibration and baryon densities attainable in relativistic heavy-ion collisions, *Phys. Rev. C* **101**, no.2, 024915 (2020) [arXiv:1911.10872 [nucl-th]].
- [38] G. Inghirami and H. Elfner, The applicability of hydrodynamics in heavy ion collisions at  $\sqrt{s_{NN}} = 2.4-7.7$  GeV, *Eur. Phys. J. C* **82**, no.9, 796 (2022) [arXiv:2201.05934 [hep-ph]].
- [39] A. Andronic, P. Braun-Munzinger and J. Stachel, Hadron production in central nucleus-nucleus collisions at chemical freeze-out, *Nucl. Phys. A* **772**, 167 (2006) [nucl-th/0511071].
- [40] Y. B. Ivanov, Alternative Scenarios of Relativistic Heavy-Ion Collisions: II. Particle Production, *Phys. Rev. C* **87**, no.6, 064905 (2013) [arXiv:1304.1638 [nucl-th]].
- [41] Y. B. Ivanov, Alternative Scenarios of Relativistic Heavy-Ion Collisions: III. Transverse Momentum Spectra, *Phys. Rev. C* **89**, no.2, 024903 (2014) [arXiv:1311.0109 [nucl-th]].
- [42] Z. W. Lin, C. M. Ko, B. A. Li, B. Zhang and S. Pal, A Multi-phase transport model for relativistic heavy ion collisions, *Phys. Rev. C* **72**, 064901 (2005) [arXiv:nucl-th/0411110 [nucl-th]].
- [43] Z. W. Lin, Evolution of transverse flow and effective temperatures in the parton phase from a multi-phase transport model, *Phys. Rev. C* **90**, no.1, 014904 (2014) [arXiv:1403.6321 [nucl-th]].
- [44] Y. B. Ivanov and A. A. Soldatov, Vorticity in heavy-ion collisions at the JINR Nuclotron-based Ion Collider fAcility, *Phys. Rev. C* **95**, no.5, 054915 (2017) [arXiv:1701.01319 [nucl-th]].
- [45] Y. B. Ivanov and A. A. Soldatov, Vortex rings in fragmentation regions in heavy-ion collisions at  $\sqrt{s_{NN}} = 39$  GeV, *Phys. Rev. C* **97**, no.4, 044915 (2018) [arXiv:1803.01525 [nucl-th]].
- [46] X. L. Xia, H. Li, Z. B. Tang and Q. Wang, Probing vorticity structure in heavy-ion collisions by local  $\Lambda$  polarization, *Phys. Rev. C* **98**, 024905 (2018) [arXiv:1803.00867 [nucl-th]].
- [47] M. A. Lisa, J. G. P. Barbon, D. D. Chinellato, W. M. Serenone, C. Shen, J. Takahashi and G. Torrieri, Vortex rings from high energy central p+A collisions, *Phys. Rev. C* **104**, no.1, 011901 (2021) [arXiv:2101.10872 [hep-ph]].
- [48] Y. B. Ivanov, Vortex rings in heavy-ion collisions at energies  $\sqrt{s_{NN}}=3-30$  GeV and possibility of their observation, *Phys. Rev. C* **107**, no.2, L021902 (2023) [arXiv:2211.17190 [nucl-th]].
- [49] N. S. Tsegelnik, E. E. Kolomeitsev and V. Voronyuk, Helicity and vorticity in heavy-ion collisions at energies available at the JINR Nuclotron-based Ion Collider facility, *Phys. Rev. C* **107**, no.3, 034906 (2023) [arXiv:2211.09219 [nucl-th]].
- [50] K. A. Maslov, E. E. Kolomeitsev and D. N. Voskresensky, Relativistic Mean-Field Models with Scaled Hadron Masses and Couplings: Hyperons and Maximum Neutron Star Mass, *Nucl. Phys. A* **950**, 64-109 (2016) [arXiv:1509.02538 [astro-ph.HE]].
- [51] K. A. Maslov, E. E. Kolomeitsev and D. N. Voskresensky, Solution of the Hyperon Puzzle within a Relativistic Mean-Field Model, *Phys. Lett. B* **748**, 369-375 (2015) [arXiv:1504.02915 [astro-ph.HE]].
- [52] N. Hornick, L. Tolos, A. Zacchi, J. E. Christian and J. Schaffner-Bielich, Relativistic parameterizations of neutron matter and implications for neutron stars, *Phys. Rev. C* **98**, no.6, 065804 (2018) [erratum: *Phys. Rev. C* **103**, no.3, 039902 (2021)] [arXiv:1808.06808 [astro-ph.HE]].
- [53] Y. Sun, Z. Zhang, C. M. Ko and W. Zhao, Evolution of  $\Lambda$  polarization in the hadronic phase of heavy-ion collisions, *Phys. Rev. C* **105**, no.3, 034911 (2022) [arXiv:2112.14410 [nucl-th]].
- [54] X. Y. Wu, C. Yi, G. Y. Qin and S. Pu, Local and global polarization of  $\Lambda$  hyperons across RHIC-BES energies: The roles of spin hall effect, initial condition, and baryon diffusion, *Phys. Rev. C* **105**, no.6, 064909 (2022) [arXiv:2204.02218 [hep-ph]].
- [55] A. Akridge, D. Gallimore, H. Morales and J. Liao, Initial Baryon Stopping and Angular Momentum in Heavy-Ion Collisions, [arXiv:2504.02192 [nucl-th]].
- [56] Y. B. Ivanov, Baryon Stopping as a Probe of Deconfinement Onset in Relativistic Heavy-Ion Collisions, *Phys. Lett. B* **721**, 123-130 (2013) [arXiv:1211.2579 [hep-ph]].
- [57] Y. B. Ivanov and D. Blaschke, Robustness of the Baryon-Stopping Signal for the Onset of Deconfinement in Relativistic Heavy-Ion Collisions, *Phys. Rev. C* **92**, no.2, 024916 (2015) [arXiv:1504.03992 [nucl-th]].
- [58] S. Z. Belen'kji and L. D. Landau, Hydrodynamic theory of multiple production of particles, *Nuovo Cim.* **3** (Suppl.

- 1), 15–31 (1956), doi:10.1007/BF02745507
- [59] Y. B. Ivanov and A. A. Soldatov, Correlation between global polarization, angular momentum, and flow in heavy-ion collisions, *Phys. Rev. C* **102**, no.2, 024916 (2020) [arXiv:2004.05166 [nucl-th]].
  - [60] Z. F. Jiang, X. Y. Wu, S. Cao and B. W. Zhang, Directed flow and global polarization in Au+Au collisions across energies covered by the beam energy scan at RHIC, *Phys. Rev. C* **107**, no.3, 034904 (2023) [arXiv:2301.02960 [nucl-th]].
  - [61] Z. F. Jiang, X. Y. Wu, S. Cao and B. W. Zhang, Hyperon polarization and its relation with directed flow in high-energy nuclear collisions, *Phys. Rev. C* **108**, no.6, 064904 (2023) [arXiv:2307.04257 [nucl-th]].
  - [62] V. Troshin, Global Polarization of  $\Lambda$  Hyperons and Its Correlation with the Directed Flow at NICA Energies, *Phys. Part. Nucl.* **55**, no.4, 1161-1165 (2024)
  - [63] <http://ckp.nrcki.ru/>.